

The Black Box Multigrid Numerical Homogenization Algorithm

J. David Moulton, Joel E. Dendy Jr., and James M. Hyman

Theoretical Division, Los Alamos National Laboratory, Los Alamos, New Mexico 87545

E-mail: moulton@lanl.gov

Received March 31, 1997; revised December 12, 1997

In mathematical models of flow through porous media, the coefficients typically exhibit severe variations in two or more significantly different length scales. Consequently, the numerical treatment of these problems relies on a *homogenization* or *upsampling* procedure to define an approximate coarse-scale problem that adequately captures the influence of the fine-scale structure. Inherent in such a procedure is a compromise between its computational cost and the accuracy of the resulting coarse-scale solution. Although techniques that balance the conflicting demands of accuracy and efficiency exist for a few specific classes of fine-scale structure (e.g., fine-scale periodic), this is not the case in general. In this paper we propose a new, efficient, numerical approach for the *homogenization* of the permeability in models of single-phase saturated flow. Our approach is motivated by the observation that multiple length scales are captured automatically by robust multilevel iterative solvers, such as Dendy's *black box multigrid*. In particular, the operator-induced variational coarsening in black box multigrid produces coarse-grid operators that capture the essential coarse-scale influence of the medium's fine-scale structure. We derive an explicit local, cell-based, approximate expression for the symmetric, 2×2 homogenized permeability tensor that is defined implicitly by the black box coarse-grid operator. The effectiveness of this black box multigrid numerical homogenization method is demonstrated through numerical examples. © 1998 Academic Press

Key Words: porous media; permeability; numerical analysis; homogenization; multigrid.

1. INTRODUCTION

The mathematical modeling of flow in porous media plays a fundamental role in the forecasting of petroleum reservoir performance, groundwater supply, and subsurface contaminant flow. A critical underlying problem in the numerical treatment of these models is the multiscale structure of heterogeneous geological formations. For example, the length

scales observed in sedimentary laminae range from the millimeter scale upward, while the simulation domain may be on the order of hundreds of meters [1]. As a result, a naive fine-scale discretization of the mathematical model is computationally intractable, yet the fine-scale variations of the model's parameters (e.g., structure and orientation of laminae) significantly affect the coarse-scale properties of the solution (e.g., average flow rates). Thus, an accurate and efficient numerical treatment of these problems relies on a *homogenization* or *upscaling* procedure to define an approximate mathematical model in which the *effective* properties of the medium vary on a coarse scale suitable for efficient computation while preserving certain coarse-scale properties of the fine-scale solution.

The inherent complexity of the homogenization process stems from the competing numerical objectives of accuracy and efficiency. This competition, and the typical compromises that result, are clearly demonstrated in the numerical treatment of the model for single-phase saturated flow that is given by [2],

$$\mathbf{u} = -\mathcal{K}(\mathbf{r})\nabla p, \quad (1a)$$

$$\nabla \cdot \mathbf{u} = Q(\mathbf{r}), \quad (1b)$$

where Eq. (1a) defines the Darcy velocity \mathbf{u} and Eq. (1b) is a mass balance relation governing the pressure p and the source-sink term $Q(\mathbf{r})$. The permeability $\mathcal{K}(\mathbf{r})$ (which may be interpreted as the mobility, hydraulic conductivity, or diffusivity) is, in general, highly variable over a significant range of length scales.

The homogenization of the diffusion operator, and hence the permeability in Eq. (1), has been studied extensively over the past 50 years [3–5]. A review of this literature for single-phase saturated flow is given by Wen and Gómez-Hernández [6]. Unfortunately, existing homogenization methods balance the numerical objectives of accuracy and efficiency only over a small class of fine-scale structures. Consequently, the increasing use of geostatistical techniques to infer physically meaningful fine-scale realizations of heterogeneous geological structure from sparse and inherently multiscale measurement data [7, 8] has generated a renewed interest in developing accurate and computationally efficient homogenization procedures. In this study we make the common assumption that the fine-scale permeability tensor is constant over each fine-scale cell, $\mathcal{K}(\mathbf{r}) = \mathcal{K}_{i,j}$ for all $\mathbf{r} \in F_{i,j}$. The objective of a homogenization procedure for Eq. (1) is to define an equivalent coarse-scale permeability tensor that is constant over each coarse-scale cell, $\widehat{\mathcal{K}}(\mathbf{r}) = \widehat{\mathcal{K}}_{i,j}$ for all $\mathbf{r} \in C_{i,j}$, and that preserves certain coarse-scale properties of the fine-scale solution (see Fig. 1).

The majority of existing homogenization methods of upscaling involve local fine-scale computations and may be classified as either *additive* or *Laplacian*. Additive methods assume that the equivalent coarse-scale permeability may be defined as an explicit function of the fine-scale permeability. In fact, in one dimension, $\widehat{\mathcal{K}}$ is given by the harmonic mean [3, 5]. Although this specific result does not extend to the multidimensional case, there are multidimensional heterogeneous structures for which additive upscaling is exact. For example, in two dimensions, if the fine-scale permeability is given by a log-normal distribution, then $\widehat{\mathcal{K}}$ is equal to the geometric mean [9]. These isolated theoretical results in combination with the low computational cost of additive methods have enticed a number of researchers to consider their widespread application (e.g., [10–13]). It was concluded that, in general, there is no single rudimentary average that defines the exact *effective* permeability [6].

This unfortunate result is a consequence of the interaction of different length scales. In particular, a fine-scale isotropic permeability may give rise to a coarse-scale anisotropic

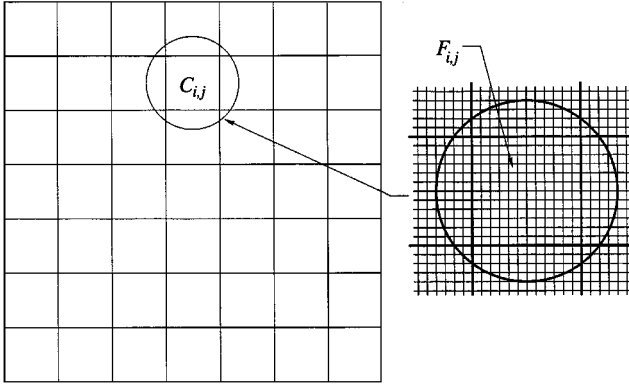


FIG. 1. The permeability tensor of a porous medium is specified on each fine-scale cell $F_{i,j}$ and must be upscaled or homogenized over each coarse-scale or computational cell $C_{i,j}$.

flow [1, 14, 15]. For example, consider an essentially one-dimensional structure in two dimensions, such as a layered medium. If the layers are aligned with the coordinate axis then the flow perpendicular to the layers encounters an effective permeability $\hat{\mathcal{K}}_{\perp}$ that is given by the harmonic mean; however, flow that is parallel with the layers encounters an effective permeability $\hat{\mathcal{K}}_{\parallel}$ that is given by the arithmetic mean. These means may differ by orders of magnitude, and hence, in this case the effective anisotropic permeability is a diagonal tensor. Moreover, if the layered structure were not aligned with the coordinate axis the effective permeability would be a full tensor. At present, no additive homogenization method is able to produce a full coarse-scale permeability tensor from a fine-scale isotropic permeability; yet ignoring the potential coarse-scale anisotropy may lead to significant errors in the simulated flows.

In contrast, most Laplacian homogenization methods are capable of constructing full coarse-scale permeability tensors, even from an isotropic fine-scale permeability. These methods use the solution of local fine-scale problems (i.e., solve Eq. (1) over a coarse-scale cell $C_{i,j}$) to infer the coarse-scale permeability tensor $\hat{\mathcal{K}}_{i,j}$ of the medium. Ideally, the boundary conditions for these local fine-scale problems would be consistent with the global fine-scale solution, but the global fine-scale solution is unknown. Consequently, artificial internal boundary conditions must be introduced, possibly corrupting the global coarse-scale behavior of the solution. In an effort to minimize the influence of the artificial boundary conditions Gómez-Hernández [16] defined the local fine-scale problems over a larger domain composed of the computational cell $C_{i,j}$ and its surrounding skin (i.e., half the annulus of neighboring coarse-scale cells). Although this method was found to perform well for a variety of heterogeneous formations [17], it does not explicitly enforce the coarse-scale permeability tensor to be symmetric and positive definite [14], and hence, it could generate nonphysical flows.

Although the physical approach of Laplacian methods may seem ad hoc, in general, they may be viewed as approximations of a rigorous two-scale asymptotic analysis. This analysis, which has been presented by a number of authors [3, 4, 18], and for which an excellent introduction is given by Holmes [19], is asymptotically exact for fine-scale periodic and nearly periodic (i.e., nonuniformly periodic) problems. Specifically, for fine-scale periodic media the homogenized permeability is a constant, symmetric, positive definite tensor that may be expressed in terms of the solution of a single, local fine-scale problem with

periodic boundary conditions. Bourgat [20] conducted a numerical study of this asymptotic analysis, demonstrating that not only was the exact coarse-scale permeability tensor symmetric positive definite, but also that a dense tensor may result from a fine-scale isotropic heterogeneity.

However, this asymptotic analysis is strictly valid only for media in which two distinct length scales exist. Although this is true for some porous media (e.g., some sedimentary laminae), it is not true in general. Durlofsky [14] investigated both the assumption of a periodic fine-scale structure and the importance of two distinct length scales in numerical simulations of flow through two-scale and multiscale heterogeneous structures. His results indicate that this approach provides an excellent coarse-scale model of a porous medium, provided that the computational scale is much larger than the fine-scale. Thus, the most serious drawback of this approach and of Laplacian methods in general, is the computational cost associated with the solution of local fine-scale flow problems on each computational cell of the global domain.

One method that attempts to bridge the gap between the low computational cost of additive methods and the superior accuracy of Laplacian methods is based on a numerical multilevel *renormalization* approach [21]. Specifically, renormalization uses the analogy of resistor networks to approximate an effective diagonal permeability tensor for a 2×2 block of fine-scale cells. Applying this technique recursively, a finite number of steps results in an equivalent diagonal permeability tensor for each coarse-scale cell $C_{i,j}$. Thus, the computational cost is comparable to additive methods, and moreover, the method automatically handles anisotropies that are aligned with the coordinate axes. However, there are two significant weaknesses. First, the resistor analogy implicitly defines artificial boundary conditions that impose one-dimensional flows in each of the coordinate directions. These artificial boundary conditions are applied at each step in the recursion and therefore may generate significant errors in the homogenized permeability [22]. Second, the homogenized permeability is at most a diagonal tensor, and hence, for cases in which the principle axes of diffusion are not aligned with the coordinate axes, the errors may be severe.

The objective of this research is to create new, computationally efficient numerical homogenization techniques that capture the essential features of the rigorous asymptotic analysis (i.e., symmetric positive definite tensor) and therefore lead to significant improvements in the numerical modeling of multiscale problems in general. To this end, we make the observation that equivalent multiscale issues arise in the development of multilevel iterative solvers. In particular, the efficiency of a multigrid method is tightly coupled to both the coarse-grid operator's approximation of the fine-grid operator's coarse-scale influence and the ability of the intergrid transfer operators to approximate the interaction of the various scales. Early work in multigrid methods considered using simple averages, such as the arithmetic and harmonic average, to define the coarse-grid operators, in conjunction with standard intergrid transfer operators (i.e., full weight restriction, bilinear interpolation). Not surprisingly, this approach was fragile, yielding convergence rates that were strongly dependent on the fine-scale structure and variability of the permeability [23]. Considerable research in this area eventually led to robust and efficient multigrid solvers, such as Dendy's black box multigrid [24, 25], strongly suggesting that the corresponding coarse-grid operators provide an excellent approximation of the homogenized operators.

Therefore, the objective of a multigrid numerical homogenization algorithm is to obtain an approximation of the homogenized permeability tensor directly from the operator-induced variationally coarsened coarse-grid operator, and most importantly, without solving a single

elliptic problem. Specifically, consider successively applying operator-induced variational coarsening to a fine-scale discretization of Eq. (1) until a coarse-scale suitable for numerical simulation is reached. On this simulation-scale an approximation of the spatially dependent homogenized permeability tensor may be obtained directly from the coarse-grid operators. This approximate multigrid homogenized permeability, $\widehat{\mathcal{K}}^{(mg)}(\mathbf{r})$, which is piecewise constant on the simulation-scale cells, may be used to define the simulation-scale (coarse-scale) model.

In Section 2.1 we review the motivation of variational coarsening and discuss its influential role (Section 2.2) in the *operator-induced* variational coarsening of black box multigrid. In Section 2.3 we derive the key result: a local, explicit expression that defines the 2×2 cell-based permeability tensor in terms of a given black box coarse-grid operator. The homogenization algorithms that are based on this local result are presented in Section 3 for both the periodic and general case. Recently, Knapik [26, 27] addressed multilevel homogenization in an alternative manner and we comment on his approach in Section 3.1. A numerical study of the periodic case is presented in Section 4 that highlights the strengths of the new black box multigrid homogenization method. Specifically, in Section 4.1, we verify that this technique is exact for problems in which the permeability has an essentially one-dimensional structure that is aligned with the coordinate axes. In this sense, it is comparable to modern renormalization. But in addition (Section 4.2), we demonstrate that this technique provides an excellent approximation of the homogenized permeability tensors that appear in Bourgat's numerical study of truly two-dimensional problems, including the computation of a dense tensor that arises from a fine-scale isotropic problem.

2. HOMOGENIZATION AND BLACK BOX MULTIGRID

To motivate the derivation of our key result, Theorem 2.1, we first review variational coarsening and then discuss the operator-induced variational coarsening that is employed in black box multigrid. We assume that the reader is familiar with the basic elements of a multigrid iterative algorithm, which are introduced in [28] and are covered in detail by a number of researchers (e.g., [29, 30]).

2.1. Variational Coarsening

A crucial aspect of any multigrid algorithm is the definition of the coarse grid operators,

$$L_k = \text{discrete operator on grid } k, \quad k = 1, 2, \dots, (\text{number of grids}) - 1$$

and the intergrid transfer operators,

$$\begin{aligned} I_{k-1}^k &= \text{interpolation operator, } \text{grid } (k-1) \rightarrow \text{grid } k \\ J_k^{k-1} &= \text{restriction operator, } \text{grid } k \rightarrow \text{grid } (k-1). \end{aligned}$$

Variational coarsening offers one means of defining L_{k-1} in terms of L_k , J_k^{k-1} , and I_{k-1}^k . The development is given by Brandt [31] and follows naturally upon the restatement of the linear system,

$$L_k p^k = Q_k, \tag{2}$$

as an equivalent minimization problem. Specifically, because L_k is symmetric positive definite we have

$$p^k = \min_{\phi \in \mathfrak{H}^{N \times M}} \left\{ \Phi(\phi) = \frac{1}{2} \phi^T L_k \phi - Q_k^T \phi \right\}. \quad (3)$$

If φ^k is an approximate solution of Eq. (3), obtained by sufficiently many relaxations of Eq. (2), the associated error $e^k = p^k - \varphi^k$ is smooth. Therefore, the objective is to use a coarse-grid approximation of the fine-grid error, $e^k = I_{k-1}^k e^{k-1}$. This is accomplished by writing

$$p^k = \varphi^k + I_{k-1}^k e^{k-1},$$

suggesting that we choose e^{k-1} to minimize $\Phi(\varphi^k + I_{k-1}^k e^{k-1})$. In this case, the equivalent linear system may be written in the form

$$L_{k-1} e^{k-1} = (J_k^{k-1} L_k I_{k-1}^k) e^{k-1} = J_k^{k-1} (Q_k - L_k \varphi^k) = Q_{k-1}. \quad (4)$$

Thus, if $J_k^{k-1} = (I_{k-1}^k)^*$, then

$$L_{k-1} = (I_{k-1}^k)^* L_k I_{k-1}^k \quad (5)$$

is symmetric. Equation (5) is typically referred to as the variational definition of the coarse-grid operator L_{k-1} .

It is common practice to employ a bilinear finite element basis for both the test and trial spaces in problems of linear diffusion; therefore, bilinear interpolation seems natural for I_{k-1}^k . However, bilinear interpolation does not yield an efficient multigrid solver for many practical applications in which the permeability (or components of the permeability tensor) varies discontinuously by orders of magnitude. In these cases one must employ an alternative interpolation scheme, such as the *operator-induced interpolation* of Dendy [24].

2.2. The Stencil and Coarse-Grid Operators

Operator-induced variational coarsening was introduced in [23] as a robust means of defining a complete set of coarse-grid and intergrid transfer operators based solely on the fine-grid discrete operator L_h . In essence, operator-induced coarsening is variational coarsening with the interpolation operator, I_{k-1}^k , defined in terms of the discrete operator L_k . Thus, we first introduce the compass-based notation of Fig. 2a as a means of conveniently describing a 9-point stencil centered at a point (i, j) on grid k . However, because the discrete operator is symmetric, the mesh itself may be viewed as an undirected graph (missing diagonal edges for a 9-point stencil, complete for the standard 5-point stencil) of the corresponding matrix. Thus, it is only necessary to store five stencil weights for a 9-point stencil and three for a 5-point. Dendy [24] chose to employ a cell-based definition of these five weights (Fig. 3), so that the 9-point stencil takes the form shown in Fig. 2b. Note that this black box multigrid code explicitly includes the negative sign that is generally present in the eight neighboring stencil weights.

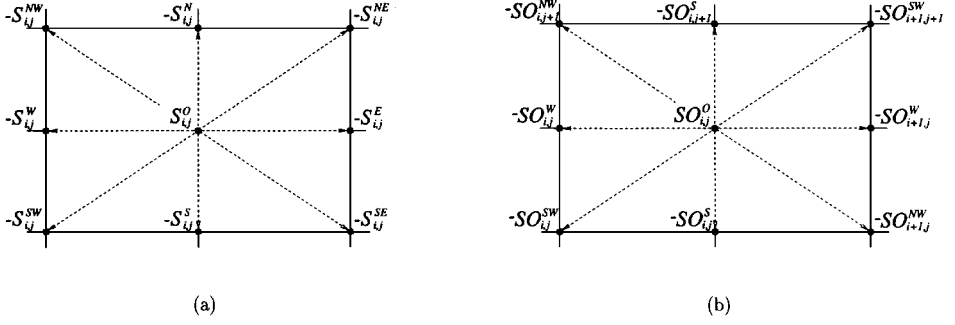


FIG. 2. (a) A compass-based definition of an arbitrary 9-point stencil. (b) A 9-point symmetric stencil defined using a cell-based nomenclature.

To define the interpolation operator, we first note that coarse-grid points that are contained in the fine grid are simply interpolated by injection:

$$(I_{k-1}^k \psi^{k-1})_{i,j} = \psi_{ic,jc}^{k-1}.$$

Another special case is horizontal lines of the coarse grid embedded in the fine grid. In this case, the primary objective is to perform piecewise linear interpolation in a manner that enforces the continuity of the normal flux and yet only uses information from the fine-grid stencil. Specifically, it may be shown (see Appendix B) that collapsing the stencil components vertically generates the interpolation

$$(I_{k-1}^k \psi^{k-1})_{i,j} = \left(\widetilde{SO}_{i,j}^{W(k)} \psi_{ic,jc}^{k-1} + \widetilde{SO}_{i+1,j}^{W(k)} \psi_{ic+1,jc}^{k-1} \right) / \widetilde{SO}_{i,j}^{O(k)}, \quad (6)$$

where the interpolation weights,

$$\widetilde{SO}_{i,j}^{W(k)} = SO_{i,j}^{W(k)} + SO_{i,j}^{SW(k)} + SO_{i,j+1}^{NW(k)},$$

$$\widetilde{SO}_{i,j}^{O(k)} = SO_{i,j}^{O(k)} - SO_{i,j}^{S(k)} - SO_{i,j+1}^{S(k)},$$

approximate this continuity condition.

An analogous treatment is employed for the vertical lines embedded in the fine grid. Finally, all that remains are fine-grid points that are centered in coarse-grid cells. In this case, the fine-grid stencil is readily inverted, because all eight neighboring corrections have

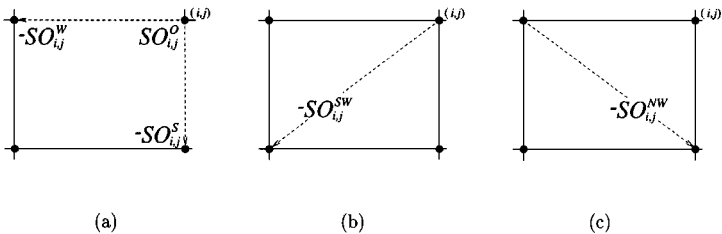


FIG. 3. The cell-based unique stencil weight definitions adopted in [24].

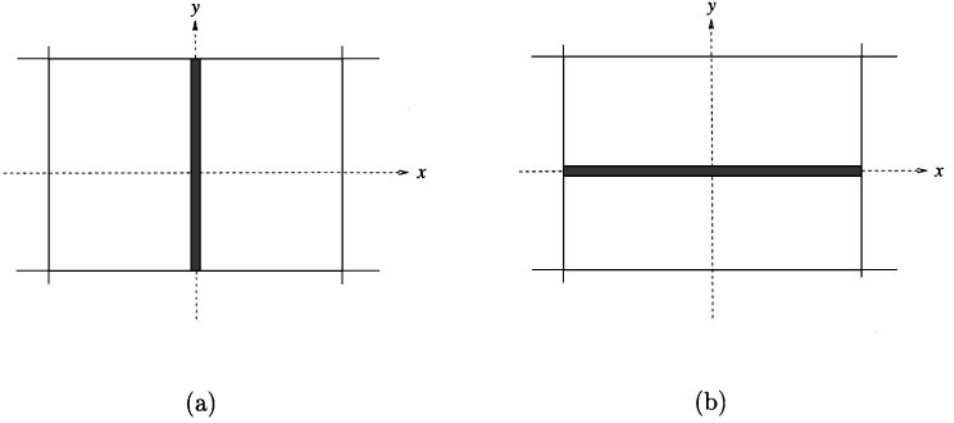


FIG. 4. The *local* flux analysis approximates: (a) the x -component of the flux and (b) the y -component of the flux, through the cell using the stencil weights.

already been evaluated:

$$\begin{aligned}
 (I_{k-1}^k \psi^{k-1})_{i+1,j+1} = & \{ SO_{i+1,j+1}^{W(k)} (I_{k-1}^k \psi^{k-1})_{i,j+1} + SO_{i+2,j+1}^{W(k)} (I_{k-1}^k \psi^{k-1})_{i+2,j+1} \\
 & + SO_{i+1,j+1}^{S(k)} (I_{k-1}^k \psi^{k-1})_{i+1,j} + SO_{i+1,j+2}^{S(k)} (I_{k-1}^k \psi^{k-1})_{i+1,j+2} \\
 & + SO_{i+1,j+1}^{SW(k)} (\psi^{k-1})_{ic,jc} + SO_{i+2,j+2}^{SW(k)} (\psi^{k-1})_{ic+1,jc+1} \\
 & + SO_{i+1,j+2}^{NW(k)} (\psi^{k-1})_{ic,jc+1} + SO_{i+2,j+1}^{NW(k)} (\psi^{k-1})_{ic+1,jc} \} / SO_{i+1,j+1}^{O(k)}. \quad (7)
 \end{aligned}$$

Using this definition of the interpolation operator, I_{k-1}^k , in the variational definition of the coarse-grid operator, L_{k-1} , Eq. (5), yields a robust multigrid algorithm that requires only the fine-grid stencil.

2.3. Extracting the Permeability Tensor

The objective of black box multigrid homogenization is to compute a constant 2×2 permeability tensor for each cell of the desired computational grid (i.e., a coarse-scale grid). However, the operator-induced coarsening of Dendy's [24] black box multigrid produces the coarse-grid discrete operator and not the permeability tensor. Thus, the underlying objective is to develop a *local* technique that extracts the cell-based permeability tensor from a coarse-grid stencil. To accomplish this objective we analyze the flux passing through the cell-centered coordinate axes shown in Fig. 4. This approach naturally relates the permeability tensor to the stencil weights because the stencil itself may be viewed as a superposition of fluxes. Specifically, we state the following theorem that we prove in Appendix A.

THEOREM 2.1. *Consider the primal conforming bilinear finite element discretization of Eq. (1) with $\mathcal{K}(x, y)$ smooth,¹ and subject to periodic boundary conditions on a rectangular*

¹Quadrature may be used to evaluate the elements of the stiffness matrix provided that it is sufficiently accurate. If we assume a smooth permeability tensor, then the quadrature must integrate cubics exactly. Alternatively, a piecewise constant sampling of the smooth permeability tensor (i.e., $\mathcal{K}(x, y) = \mathcal{K}_{i+\frac{1}{2},j+\frac{1}{2}}$ for $(x, y) \in \Omega_{i+\frac{1}{2},j+\frac{1}{2}}$) may be used, in which case only quadratics need to be integrated exactly.

domain Ω . In addition, assume a tensor-product grid with a constant grid spacing in each coordinate direction that is denoted by (hx, hy) . A second-order approximation of the permeability tensor $\mathcal{K}_{i+\frac{1}{2},j+\frac{1}{2}} = \mathcal{K}(x_{i+\frac{1}{2}}, y_{j+\frac{1}{2}})$ is given by

$$\widehat{\mathcal{K}}_{i+\frac{1}{2},j+\frac{1}{2}} = \begin{bmatrix} \frac{hx}{hy} \{ \overline{S}_{i,j}^E + S_{i,j}^{NE} + S_{i+1,j}^{NW} \} & (S_{i,j}^{NE} - S_{i+1,j}^{NW}) \\ (S_{i,j}^{NE} - S_{i+1,j}^{NW}) & \frac{hy}{hx} \{ \overline{S}_{i,j}^N + S_{i,j}^{NE} + S_{i+1,j}^{NW} \} \end{bmatrix}, \quad (8)$$

where we have defined

$$\begin{aligned} \overline{S}_{i,j}^E &= \frac{1}{2} (S_{i,j}^E + S_{i,j+1}^E), \\ \overline{S}_{i,j}^N &= \frac{1}{2} (S_{i,j}^N + S_{i+1,j}^N). \end{aligned}$$

For a constant permeability tensor (i.e., $\mathcal{K}(x, y) \equiv \mathcal{K}_{i+\frac{1}{2},j+\frac{1}{2}} \forall (x, y) \in \Omega$), Eq. (8) is an exact expression.

In the case of fine-scale periodic structures, it is well known that a two-scale asymptotic analysis (i.e., denote the slow global scale \mathbf{r} and the fast local scale $\boldsymbol{\rho} = \mathbf{r}/\epsilon$, where $\epsilon > 0$ is a small parameter) to an expression for the homogenized permeability $\widehat{\mathcal{K}}^{(as)}$ [3, 4]. Moreover, it has been shown that $\widehat{\mathcal{K}}^{(as)}$ is a constant and symmetric positive definite tensor that is not, in general, an explicit function of $\widehat{\mathcal{K}}(\boldsymbol{\rho})$, but depends on specific solutions of the local fine-scale problem

$$-\nabla_{\boldsymbol{\rho}} \cdot [\mathcal{K}(\boldsymbol{\rho}) \nabla_{\boldsymbol{\rho}} \phi] = 0, \quad (9)$$

for $\boldsymbol{\rho} \in F$ and with ϕ periodic on F .

Therefore to use operator-induced variational coarsening to perform an approximate numerical multigrid homogenization of a fine-scale periodic permeability we must relate the fine-scale discretization of Eq. (9), the results of the coarsening procedure, and Theorem 2.1. These relations are summarized in the following theorem.

THEOREM 2.2. *Consider a 9-point vertex-based consistent discretization of Eq. (9) over Ω_n (the n -times periodic extension of F for integer $n > 3$). Furthermore, assume a tensor-product grid that has a constant grid spacing in each coordinate direction denoted by (hx, hy) . Applying operator-induced variational coarsening until the stencil at each point on the coarse-grid is identical leads to a coarse-grid operator that is second-order consistent with a constant coefficient elliptic PDE*

$$-\nabla_{\boldsymbol{\rho}} \cdot [\widehat{\mathcal{K}}^{(bb)} \nabla_{\boldsymbol{\rho}} \phi] = 0, \quad (10)$$

with ϕ periodic on Ω_n . Moreover, the black box multigrid homogenized permeability $\widehat{\mathcal{K}}^{(bb)}$ is given by Eq. (8).

Proof. It is straightforward to show that the important properties of the fine-grid stencil, namely, that it is conservative (i.e., zero sum) and symmetric, are preserved under operator-induced variational coarsening. Furthermore, each point has an identical stencil, therefore, periodicity implies the discretization is consistent with some constant-coefficient PDE. Thus, the coarse-scale solution is smooth and moreover, its Taylor series expansion about any vertex readily yields Eq. (10) with $\widehat{\mathcal{K}}^{(bb)}$ given by Eq. (8). \blacksquare

Although we focus on fine-scale periodic media in this preliminary investigation, the ultimate objective is the efficient numerical homogenization of general fine-scale permeability over a global domain subject to general boundary conditions. A two-scale asymptotic analysis has been applied to nonuniformly periodic structures (i.e., $\mathcal{K}(\mathbf{r}, \boldsymbol{\rho})$ is a function of both the slow and fast scales) revealing that, in general, the homogenized permeability will vary on the slow scale [3, 4]. The unfortunate consequence of this spatial dependence is that to characterize the homogenized permeability a continuum of local fine-scale elliptic problems must be solved.

We are optimistic that the extension of multigrid numerical homogenization to general fine-scale structures will provide an efficient and accurate numerical approximation of the spatially dependent homogenized permeability tensor. The key components of this extension are summarized in the following conjecture.

Conjecture 2.1. Consider the conforming bilinear finite element stencil specified in Theorem 2.1. Applying operator-induced variational coarsening until the desired coarse-grid is reached leads to a coarse-grid operator that is consistent with an elliptic PDE of the form

$$-\nabla \cdot [\widehat{\mathcal{K}}(x, y) \nabla \phi] = \widehat{Q}(x, y), \quad (11)$$

where $\widehat{\mathcal{K}}(x, y)$ and $\widehat{Q}(x, y)$ are piecewise constant (i.e., $\widehat{\mathcal{K}}(x, y) = \widehat{\mathcal{K}}_{i+\frac{1}{2}, j+\frac{1}{2}} \mathbb{V}(x, y) \in \Omega_{i+\frac{1}{2}, j+\frac{1}{2}}$). On interior cells an approximation of the piecewise homogenized permeability tensor is given by Eq. (8).

Thus, the extension to nonperiodic problems requires a consistency relation such as that of Conjecture 2.1, as well as the extension of Theorem 2.1 to incorporate nonperiodic boundary conditions.

3. THE MULTIGRID HOMOGENIZATION ALGORITHM

3.1. The Periodic Case

To motivate the black box multigrid homogenization algorithm for the periodic case, we briefly discuss the relevant grid configuration issues. Specifically, the implementation of black box multigrid [25], and hence, the new homogenization code that was derived from it, was simplified by the use of fictitious points. Thus, if we consider the physical domain $[x_1, y_1] \times [x_{L+1}, y_{M+1}]$, periodicity requires

$$\begin{aligned} u(x_1, y) &= u(x_{L+1}, y) \quad \forall y \in (y_1, y_{M+1}) \\ u(x, y_1) &= u(x, y_{M+1}) \quad \forall x \in (x_1, x_{L+1}). \end{aligned}$$

Consequently, a typical $L \times M$ computational grid (Fig. 5) has the *top* and *right* edges composed of fictitious points. Furthermore, the smallest plausible grid is 3×3 . Thus, the homogenization of a representative cell may be accomplished by choosing the physical domain to be a 3×3 tiling of the representative cell so that the coarsest grid is composed of a 3×3 tiling of homogenized cells. For example, consider the tiling shown in Fig. 6a on which a 12×12 computational mesh is superimposed. After two coarsenings, the computational mesh is only 3×3 and the domain may be viewed as a tiling of homogenized cells (Fig. 6b). Note that the fictitious cells are displayed in lighter shades of gray.

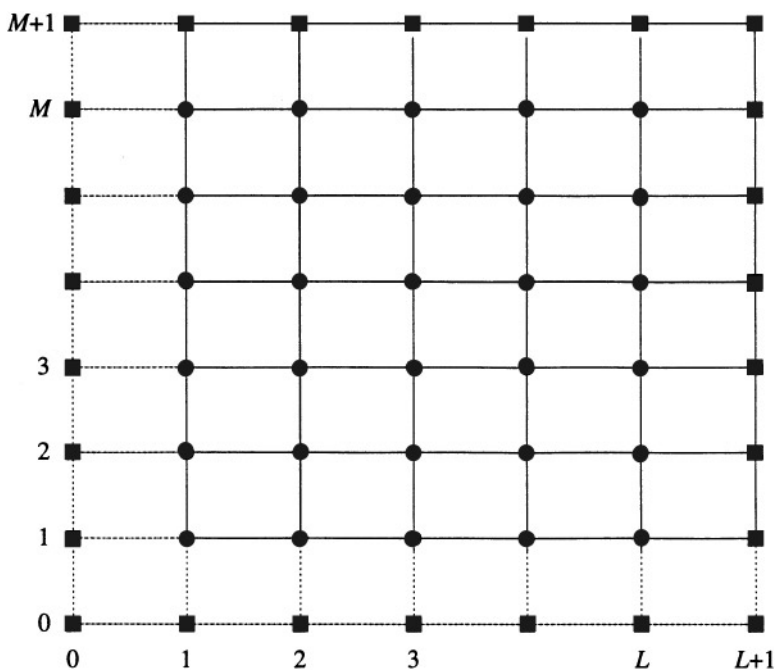


FIG. 5. A typical $L \times M$ computational mesh is shown for periodic boundary conditions with the point-wise unknowns indicated by shaded circles. The entire $(L + 2) \times (M + 2)$ mesh employed by *black box multigrid* includes the fictitious points depicted as shaded squares.

This procedure is ideal, provided that the fine-scale structure of the problem may be represented exactly on a $3 \cdot 2^{k-1} \times 3 \cdot 2^{k-1}$ mesh. However, if such a representation is not possible, using an exact representation on the finest grid becomes problematic. To clarify this point, consider vertical stripes on the representative cell (i.e., $[0, 1] \times [0, 1]$)

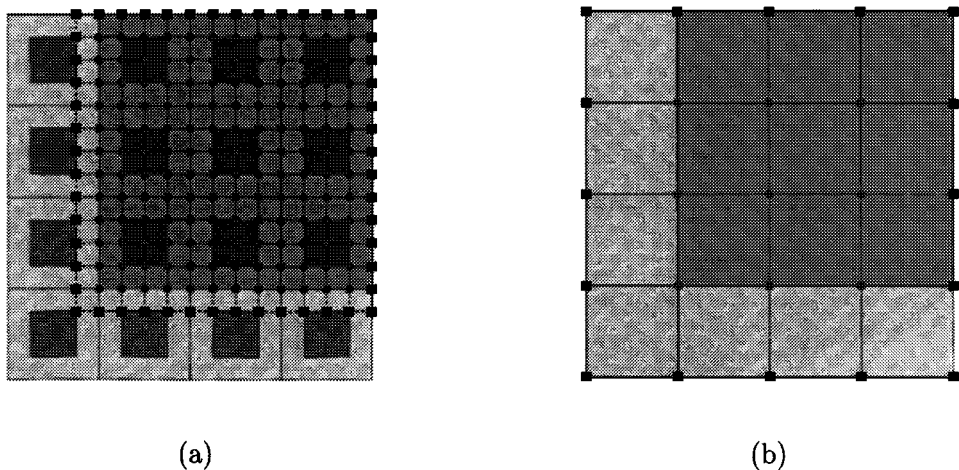


FIG. 6. (a) 12×12 computational mesh is superimposed on a 3×3 tiling of representative cells. (b) 3×3 computational mesh on the coarsest grid. The domain is now composed of homogenized cells.

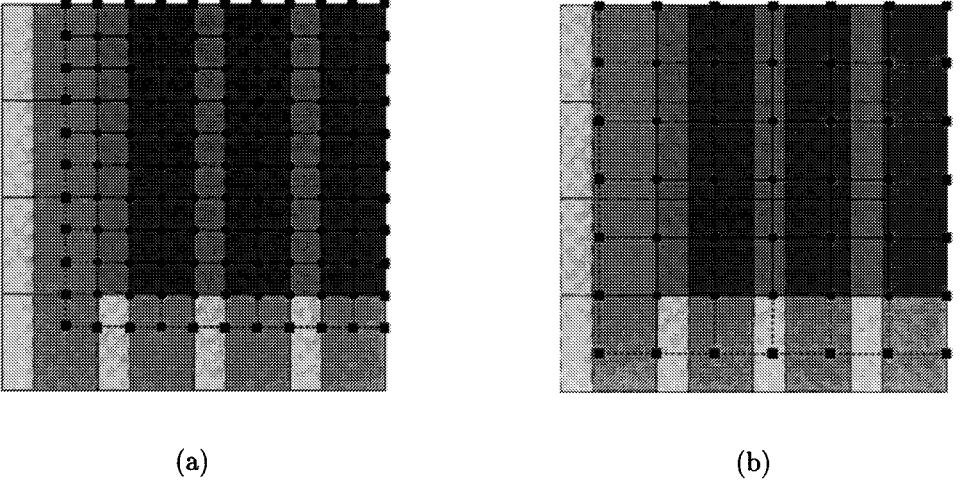


FIG. 7. (a) A fine-grid (9×9) representation of vertical stripes with $\mu_x = 1/3$. (b) After one coarsening a 5×5 grid remains that is no longer consistent with the 3×3 homogenized grid. In both cases the solid dots represent grid points and the solid squares represent fictitious points.

defined by

$$\mathcal{K}(x, y) = \begin{cases} \mathcal{K}_L, & 0 < x < \mu_x \\ \mathcal{K}_R, & \mu_x < x < 1 \end{cases},$$

which, if $\mu_x = 1/3$, may be represented exactly on the 9×9 fine grid shown in Fig. 7a. The first coarsening yields a 5×5 mesh, destroying the internal periodicity (Fig. 7b).

A number of treatments may be proposed to circumvent this problem approximately; however, because our objective is to investigate the potential of the multigrid homogenization procedure, we restrict the fine-grid representation to $3 \cdot 2^{k-1} \times 3 \cdot 2^{k-1}$ uniform meshes and employ a cell-centered, point-wise sampling of $\mathcal{K}(x, y)$. This restriction implies that the black box multigrid homogenization of fine-grid structures that are not represented exactly on this mesh should be defined by the limit of the sequence of diffusion tensors that arise as the fine-scale mesh is refined (i.e., increasing k). It is anticipated that this sequence will be first-order convergent, and this claim is demonstrated in Section 4.1.2. We summarize this homogenization procedure in the following algorithm.

ALGORITHM 3.1. Black Box Multigrid Homogenization of Periodic Problems.

1. Construct the conforming bilinear FEM stencil for a 3×3 tiling of the representative cell on a $3 \cdot 2^{k-1} \times 3 \cdot 2^{k-1}$ uniform fine grid.
2. Construct the coarse-grid operators with operator induced coarsening [25].
3. Based on Theorem 2.2, compute $\widehat{\mathcal{K}}^{(bb)}$ on the 3×3 grid (i.e., the coarsest grid).
4. Is the fine-scale structure of the representative cell captured adequately on the fine grid (i.e., either exactly or evidenced by satisfactory convergence of $\widehat{\mathcal{K}}^{(bb)}$)?
 YES: the black box multigrid homogenized diffusion tensor $\equiv \widehat{\mathcal{K}}^{(bb)}$
 NO: increase k and goto 1.

An alternative vertex-based approach is considered in [26, 27] which inverts a 9×9 system that is defined over a group of four cells. These methods result in equivalent homogenized

permeability tensors if the stencil is spatially constant, in which case it is natural to assume that the four neighboring cells will have identical properties. However, in the general case (Section 3.2), this assumption may be too restrictive, and therefore, we feel that a local technique is preferable.

3.2. The General Case

The objective in the general case is somewhat different. Here it is assumed that a multiscale diffusion problem is readily defined on a fine scale but that practical computations are limited to a much coarser scale. Thus, we first note that Conjecture 2.1 applies on all interior cells. Moreover, the extension of Theorem 2.1 to the case of homogeneous Neumann boundary conditions is straightforward because these boundary conditions are the natural ones for the variational formulation. Unfortunately, Dirichlet and mixed boundary conditions require careful attention. These extensions are beyond the scope of this preliminary investigation; hence, we propose the following algorithm for the general case but do not evaluate its potential.

ALGORITHM 3.2. Black Box Multigrid Homogenization of General Problems.

1. *Construct the conforming bilinear FEM stencil on a fine grid whose spacing corresponds to the fine scale of the modeling problem*
2. *Construct the coarse-grid operators with operator-induced coarsening [24] so that the coarsest grid is the desired computational grid.*
3. (a) *Based on Conjecture 2.1, use Eq. (8) to compute $\widehat{\mathcal{K}}_{i+\frac{1}{2},j+\frac{1}{2}}^{(bb)}$ for all interior cells on the coarsest grid.*
 (b) *Based on the necessary extension of both Conjecture 2.1 and Theorem 2.1 compute $\widehat{\mathcal{K}}_{i+\frac{1}{2},j+\frac{1}{2}}^{(bb)}$ for all boundary cells on the coarsest grid.*
4. *Store $\widehat{\mathcal{K}}_{i+\frac{1}{2},j+\frac{1}{2}}^{(bb)}$ for future use.*

4. NUMERICAL EXAMPLES

To explore the potential of the black box homogenization, we present numerical results for several model problems that may be divided into two subsections. The first subsection consists of the homogenization of a constant diffusivity (i.e., a fixed-point problem), various stripes (i.e., essentially one-dimensional problems), and the infamous checkerboard problem. The second subsection discusses the examples of Bourgat [20] that focus on the dependence of the permeability tensor on the shape and diffusivity of an interior inhomogeneity, $\Omega_1 \subset \Omega \equiv \{[0, 1] \times [0, 1]\}$.

4.1. A Progressive Test Suite

4.1.1. Constant Tensor

A domain having a constant permeability tensor may be viewed as the ultimate result of a homogenization procedure for which no further homogenization is desired or possible. Therefore, a constant permeability tensor must be a fixed point of the homogenization operator,

$$\mathcal{K}_{i+\frac{1}{2},j+\frac{1}{2}} = \mathcal{H}_{bb}(\mathcal{K}(x, y)) = \mathcal{H}_{bb}(\mathcal{K}_{i+\frac{1}{2},j+\frac{1}{2}}).$$

In this case we know that the stencil is preserved under variational coarsening and that by Theorem 2.1, $\widehat{\mathcal{K}}_{i+\frac{1}{2}, j+\frac{1}{2}}$ given by Eq. (8), is an exact expression. Therefore, a constant permeability tensor is a fixed point of the black box homogenization operator. This claim was also verified numerically with the black box code.

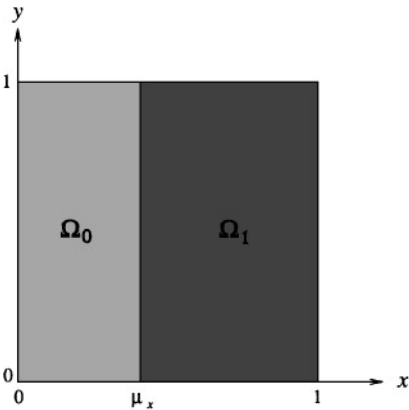
4.1.2. Stripes

Analytic homogenization results exist in one dimension making essentially one-dimensional problems (i.e., problems in which the diffusive process is completely decoupled in x and y), the first logical step beyond the simple constant permeability tensor. Specifically, the striped patterns shown in Figs. 8a and 8b are two-dimensional problems in which the material structure is only one-dimensional. If in addition, the following diagonal permeability tensor is defined,

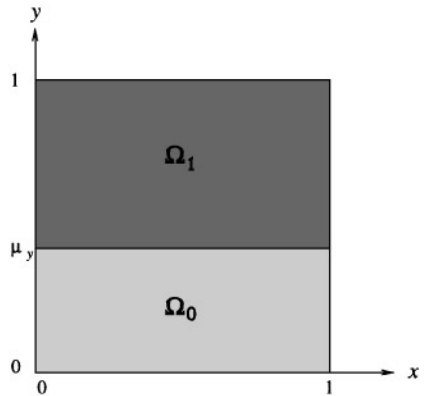
$$\mathcal{K}(x, y) = \begin{cases} \begin{bmatrix} \alpha_1 & 0 \\ 0 & \alpha_2 \end{bmatrix} & \forall (x, y) \in \Omega_0 \\ \begin{bmatrix} \beta_1 & 0 \\ 0 & \beta_2 \end{bmatrix} & \forall (x, y) \in \Omega_1 \end{cases},$$

then the permeability process is completely decoupled in x and y . Therefore, based on a one-dimensional analysis, the homogenized permeability tensor for the vertical stripes of Fig. 8a may be written

$$\widehat{\mathcal{K}} = \begin{bmatrix} \frac{\alpha_1 \beta_1}{(1 - \mu_x) \alpha_1 + \mu_x \beta_1} & 0 \\ 0 & \mu_x \alpha_2 + (1 - \mu_x) \beta_2 \end{bmatrix} \quad (12)$$



(a)



(b)

FIG. 8. Vertical and horizontal stripes.

TABLE 1

A Sequence of Homogenized Permeability Tensors Obtained with Progressively Finer Uniform Grids for Vertical Stripes with $\mu_x = 1/3$, $\alpha_1 = \alpha_2 = 3$, and $\beta_1 = \beta_2 = 50$

Fine Grid	$\widehat{\mathcal{K}}_{bb}^{(x,x)}$	$ \mathcal{K}^{(x,x)} - \widehat{\mathcal{K}}_{bb}^{(x,x)} $	$\widehat{\mathcal{K}}_{bb}^{(y,y)}$	$ \mathcal{K}^{(y,y)} - \widehat{\mathcal{K}}_{bb}^{(y,y)} $
12×12	10.1695	2.13379	38.2500	3.9167
24×24	7.27273	0.76298	32.3750	1.9583
48×48	8.48057	0.44486	35.3125	0.9792
96×96	7.88034	0.20537	33.8437	0.4896
192×192	8.14249	0.10678	34.5781	0.2448
384×384	7.98337	0.05234	34.2109	0.1224
768×768	8.06215	0.02644	34.3945	0.0612

while for the horizontal stripes of Fig. 8b it becomes

$$\widehat{\mathcal{K}} = \begin{bmatrix} \mu_y \alpha_1 + (1 - \mu_y) \beta_1 & 0 \\ 0 & \frac{\alpha_2 \beta_2}{(1 - \mu_y) \alpha_2 + \mu_y \beta_2} \end{bmatrix}. \quad (13)$$

Recalling that operator-induced interpolation is constructed in terms of transverse averaged stencil coefficients to ensure continuity of the normal current, we expect to solve these essentially one-dimensional problems exactly. Indeed this expectation is correct, provided that

$$\mu_x = i2^{-k}, \quad \mu_y = i2^{-k}, \quad (14)$$

where i, k are positive integers and $i \leq k$. This choice of μ_x and μ_y ensures that a uniform fine grid exists that not only represents the stripes exactly but also when coarsened uses the same coarse mesh in each homogenized cell (see Section 3.1). In the case of stripes that violate Eq. (14), we define the homogenized tensor as the limit of the sequence of multigrid homogenized tensors that is generated by considering successively *finer* fine-grid problems.

For example, consider vertical stripes with $\mu_x = 1/3$, $\alpha_1 = \alpha_2 = 3$, and $\beta_1 = \beta_2 = 50$ for which the corresponding sequence of black box multigrid homogenized tensors is presented in Table 1. The exact homogenized permeability tensor is readily obtained from Eq. (12),

$$\widehat{\mathcal{K}} = \begin{bmatrix} \frac{225}{28} & 0 \\ 0 & \frac{103}{3} \end{bmatrix} = \begin{bmatrix} 8.0357 & 0 \\ 0 & 34.3333 \end{bmatrix}, \quad (15)$$

and was used to compute the errors that appear in Table 1. It is apparent from the errors that this procedure is first-order convergent.

4.1.3. Checkerboard

The checkerboard (Fig. 9) is one possible representation of a granular mixture such as sand with Ω_0 denoting the grains of sand and Ω_1 denoting the intergranular space. Although this is a truly two-dimensional problem, the exact solution is well known for isotropic diagonal

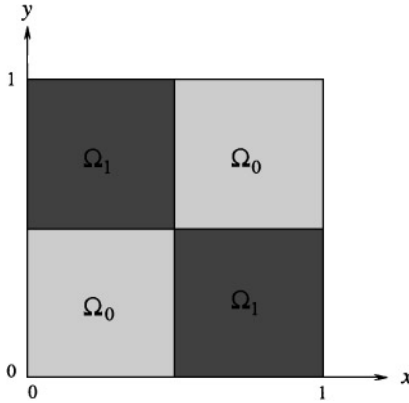


FIG. 9. The checkerboard.

tensors [4]. Specifically, with $\mathcal{K}(x, y)$ defined by

$$\mathcal{K}(x, y) = \begin{cases} \alpha \cdot I_2 & \forall (x, y) \in \Omega_0, \\ \beta \cdot I_2 & \forall (x, y) \in \Omega_1, \end{cases}$$

where I_2 is the 2×2 identity matrix. The homogenized permeability tensor is

$$\widehat{\mathcal{K}} = \sqrt{\alpha\beta} \cdot I_2.$$

A computation to evaluate the black box homogenized permeability tensor was performed with the unfortunate result:

$$\widehat{\mathcal{K}}^{(bb)} = \frac{1}{2}(\alpha + \beta) \cdot I_2.$$

It is not difficult to trace this error to its source, although it is likely nontrivial to correct it. In particular, the interpolation operator is obtained by first averaging the stencil in either x or y to define the required one-dimensional interpolation problems. This averaging necessarily defines an interpolation operator consistent with a medium having constant diffusivity given by the arithmetic mean of α and β . Moreover, taking $\beta = 1/\alpha$ reveals that the corresponding error is unbounded. At this time, it is not known how to alleviate this problem by altering the operator-induced interpolation in a manner that still preserves the 9-point, symmetric, conservative stencils under variational coarsening.

4.2. Bourgat's Examples

4.2.1. Shape Dependence

An evaluation of the geometric dependence of the homogenized permeability tensor is demonstrated with three basic shapes: square, disk, and lozenge (i.e., rotated square), which are shown in Figs. 10a–c. The permeability tensor of these representative cells is defined by

$$\mathcal{K}(x, y) = \begin{cases} 1 \cdot I_2 & \forall (x, y) \in \Omega_0 \\ 10 \cdot I_2 & \forall (x, y) \in \Omega_1 \end{cases}.$$

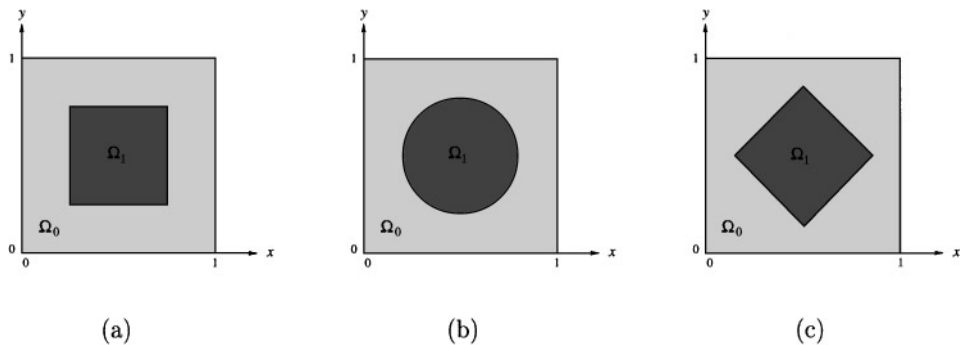


FIG. 10. Three inhomogeneities with an area of $1/4$, but different shapes.

In all cases, the area of Ω_1 is $1/4$. Moreover, symmetry ensures that the homogenized permeability tensor will also be a scalar multiple of the identity. This property was verified to hold for our numerical algorithm, and the results are displayed in Table 2. A comparison of the results that we obtained with a 768×768 fine grid and those found in [20] is summarized in Table 3, where percentage differences, relative to the square inhomogeneity, are also included. These results demonstrate that the relative sensitivity of *black box* homogenization is similar to the rigorous treatment of Bourgat. In a direct comparison the black box results consistently overestimate the asymptotic value by approximately 2–3%. This result is quite impressive when a commonly employed alternative such as the two-dimensional harmonic average not only underestimates the asymptotic value by approximately 17% but also is independent of the shape of the internal inhomogeneity.

4.2.2. Dependence on the Relative Diffusivity

In this example, we consider a square inhomogeneity (Fig. 11) defined by

$$\mathcal{K}(x, y) = \begin{cases} 1 \cdot I_2 & \forall (x, y) \in \Omega_0 \\ \lambda \cdot I_2 & \forall (x, y) \in \Omega_1 \end{cases},$$

TABLE 2

A Sequence of Homogenized Permeability Tensors Obtained with Progressively Finer Meshes for the Three Representative Cells Shown in Fig. 10

Fine grid	Square	Disk	Lozenge
12×12	1.5979	1.5979	1.5979
24×24	1.5979	1.5979	1.4182
48×48	1.5979	1.5495	1.5629
96×96	1.5979	1.5797	1.6354
192×192	1.5979	1.5676	1.6015
384×384	1.5979	1.5673	1.6175
768×768	1.5979	1.5631	1.6079

TABLE 3

Shape Dependence of the Diffusivity, Relative to the Square (i.e., the Percentage of Relative Difference—%RD) Is Presented for the Results of Bourgat [20] and Black Box Homogenization

Shape	Bourgat	% RD	Black box	% RD
Square	1.548	—	1.598	—
Disk	1.516	−2.06	1.563	−2.19
Lozenge	1.573	+1.69	1.608	+0.63

to evaluate the dependence of the homogenized permeability tensor on the parameter λ . Symmetry once again guarantees that the homogenized permeability tensor is also a scalar multiple of the identity. Unfortunately, the structure of Ω_1 cannot be described exactly on a uniform $3 \cdot 2^{k-1} \times 3 \cdot 2^{k-1}$ grid, where k is a positive integer. As a result, for each λ we obtain a convergent sequence of permeability tensors. A sample computation with $\lambda = 10$ is summarized in Table 4. For purposes of comparison, we use the results of the finest grid displayed in Fig. 12. Also appearing in Fig. 12 are the results of Bourgat [20] as well as the commonly used means,

$$\widehat{\mathcal{K}}^{(am)} = \int_0^1 \int_0^1 \mathcal{K}(x, y) dx dy = \frac{1}{9}(\lambda + 8) \cdot I_2,$$

$$\widehat{\mathcal{K}}^{(hm)} = \left[\int_0^1 \int_0^1 [\mathcal{K}(x, y)]^{-1} dx dy \right]^{-1} = \frac{9\lambda}{(1 + 8\lambda)} \cdot I_2.$$

We note the excellent agreement of the black box homogenized permeability coefficient with the asymptotic results over eight orders of magnitude in λ . We also observe that the catastrophic failure of the harmonic mean as $\lambda \rightarrow 0^+$ is in contrast with an overestimation of approximately 10% in the arithmetic mean. Moreover, as $\lambda \rightarrow +\infty$, the harmonic mean yields approximately a 10% underestimation, while the arithmetic mean grows linearly, displaying an arbitrarily large error.

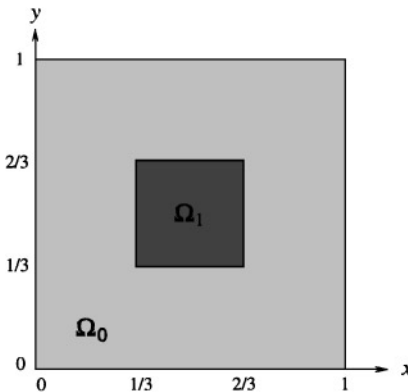


FIG. 11. A square inhomogeneity with diffusivity λ and an area of $1/9$.

TABLE 4
A Sequence of Homogenized Permeability Tensors Obtained with Progressively Finer Meshes for the Inhomogeneity Shown in Fig. 11 with $\lambda = 10$

Fine grid	$\widehat{\mathcal{K}}_{bb}^{(x,x)} = \widehat{\mathcal{K}}_{bb}^{(y,y)}$
12×12	1.5979
24×24	1.1243
48×48	1.2897
96×96	1.1934
192×192	1.2372
384×384	1.2143
768×768	1.2254

4.2.3. A Dense Homogenized Permeability Tensor

To demonstrate that an isotropic inhomogeneity may lead to a dense tensor, Bourgat [20] considered the L-shaped region shown in Fig. 13, with the permeability tensor

$$\mathcal{K}(x, y) = \begin{cases} 1 \cdot I_2 & \forall (x, y) \in \Omega_0 \\ 10 \cdot I_2 & \forall (x, y) \in \Omega_1 \end{cases}.$$

The asymptotic computation of Bourgat gives,

$$\widehat{\mathcal{K}}^{(as)} = \begin{bmatrix} 1.915 & -0.101 \\ -0.101 & 1.915 \end{bmatrix} = \mathcal{Q} \begin{bmatrix} 2.016 & 0 \\ 0 & 1.814 \end{bmatrix} \mathcal{Q}^T,$$

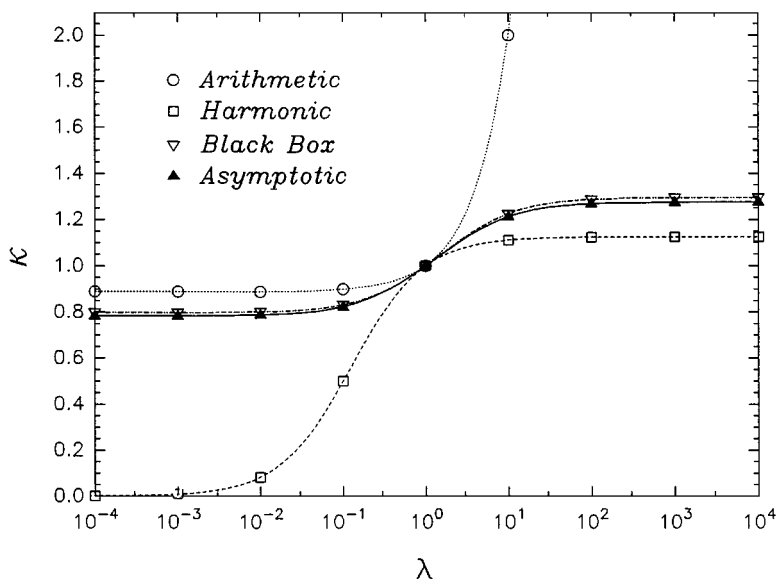


FIG. 12. Dependence of homogenized diffusivities on the relative diffusivity λ .

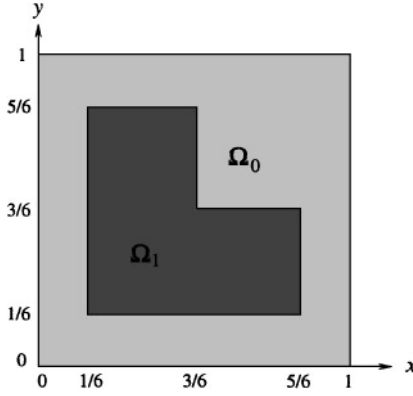


FIG. 13. The homogenization of an L-shaped inhomogeneity leads to a dense tensor.

where the matrix of eigenvectors Q is given by

$$Q = \frac{1}{\sqrt{2}} \begin{bmatrix} -1 & 1 \\ 1 & 1 \end{bmatrix}.$$

Q defines the principal axes of diffusion, in this case a rotation of 45° .

Black box homogenization also gives a full tensor; specifically, for a 768×768 fine grid (Table 5) we have

$$\widehat{\mathcal{K}}^{(bb)} = \begin{bmatrix} 1.959 & -0.153 \\ -0.153 & 1.959 \end{bmatrix} = Q \begin{bmatrix} 2.113 & 0 \\ 0 & 1.806 \end{bmatrix} Q^T.$$

Moreover, we remarkably obtain the exact principal axes of diffusion in this case. The only error is the scaling in each of these directions, approximately 5% and 0.4%, respectively.

5. CONCLUSIONS

An efficient and accurate homogenization procedure suitable for a broad class of multi-scale diffusion problems is essential and yet was previously unavailable. To this end, we

TABLE 5
A Sequence of Homogenized Permeability Tensors Obtained with Progressively Finer Meshes for the L-Shaped Inhomogeneity Shown in Fig. 13

Fine grid	$\widehat{\mathcal{K}}_{bb}^{(x,x)} = \widehat{\mathcal{K}}_{bb}^{(y,y)}$	$\widehat{\mathcal{K}}_{bb}^{(x,y)}$
12×12	1.4972	-0.08527
24×24	2.3766	-0.17604
48×48	1.8280	-0.14011
96×96	2.0515	-0.15881
192×192	1.9316	-0.15094
384×384	1.9887	-0.15519
768×768	1.9594	-0.15317

hypothesized that the robustness of Dendy's black box multigrid codes [24, 25] implied that the corresponding coarse-grid operators were accurate approximations of the true coarse-scale operators and, therefore, that the operator-induced coarsening intrinsically provided an efficient discrete multilevel homogenization procedure. Thus, we developed a local expression (Theorem 2.1, Eq. (8)) which through Algorithm 3.1 defines the black box multigrid approximation of the homogenized permeability tensor.

In the numerical tests of Section 4.2 we compared this new multilevel homogenization procedure with several examples from Bourgat's [20] numerical study. The results of these tests are very encouraging. In particular, the multigrid homogenized permeability tensor displayed the correct relative dependence on the shape of the internal inhomogeneity, a dependence missed entirely by the simple averages. The new technique also demonstrated an impressive accuracy over eight orders of magnitude in the relative diffusivity of a square inhomogeneity. Finally, the multigrid homogenization algorithm demonstrated that it can capture coarse-scale anisotropic permeability even when it arises from a fine-scale problem with isotropic permeability. Moreover, in this case the approximated permeability tensor defined the exact principal axes of diffusion with errors of 0.4% and 5% in the corresponding eigenvalues. Unfortunately, this new technique is not infallible, yielding the arithmetic mean in the case of a checkerboard problem. We feel that this is an isolated problem and are optimistic that we can prove that this is the only pathological example. In practice, a known pathology such as this may be circumvented, although ultimately we hope to rectify this problem by improving the operator-induced coarsening procedure. Hence, we are excited that research in this vein may indirectly lead to improvements in the black box code itself.

Based on these preliminary results, we are very interested in extending this work to the general case. Thus, we will be investigating the potential of Algorithm 3.2 through its application to both contrived and real world diffusive modeling problems.

APPENDIX A: PROOF OF THEOREM 2.1

A.1. A Second-Order Approximation

A local flux analysis is used to construct approximations to the x and y components of the flux at the cell center $(x_{i+\frac{1}{2}}, y_{j+\frac{1}{2}})$ by considering the contributions from each of the six stencil weights. In particular, we write

$$\begin{aligned}\mathcal{F}_{i+\frac{1}{2},j+\frac{1}{2}}^{(x)} &= \mathcal{F}_{i+\frac{1}{2},j+\frac{1}{2}}^E + \mathcal{F}_{i+\frac{1}{2},j+\frac{1}{2}}^{NE(x)} + \mathcal{F}_{i+\frac{1}{2},j+\frac{1}{2}}^{NW(x)}, \\ \mathcal{F}_{i+\frac{1}{2},j+\frac{1}{2}}^{(y)} &= \mathcal{F}_{i+\frac{1}{2},j+\frac{1}{2}}^N + \mathcal{F}_{i+\frac{1}{2},j+\frac{1}{2}}^{NE(y)} + \mathcal{F}_{i+\frac{1}{2},j+\frac{1}{2}}^{NW(y)},\end{aligned}$$

where $\mathcal{F}_{i+\frac{1}{2},j+\frac{1}{2}}^{(x)}$ is an approximation of the x -component of the flux at $(x_{i+\frac{1}{2}}, y_{j+\frac{1}{2}})$, and $\mathcal{F}_{i+\frac{1}{2},j+\frac{1}{2}}^E$, $\mathcal{F}_{i+\frac{1}{2},j+\frac{1}{2}}^{NE(x)}$, and $\mathcal{F}_{i+\frac{1}{2},j+\frac{1}{2}}^{NW(x)}$ denote the contributions from their respective stencil connections. Analogous definitions apply to the y -component.

To facilitate this analysis, we first develop the notation and coordinate systems required by these unknowns. Specifically, the evaluation of the flux at the cell center requires the partial derivatives of the solution,

$$(p_x^h)_{i+\frac{1}{2},j+\frac{1}{2}} = p_x^h|_{(x_{i+\frac{1}{2}},y_{j+\frac{1}{2}})}, \quad (p_y^h)_{i+\frac{1}{2},j+\frac{1}{2}} = p_y^h|_{(x_{i+\frac{1}{2}},y_{j+\frac{1}{2}})}.$$

For a 9-point conforming bilinear finite element stencil $p_x^h(x, y)$ and $p_y^h(x, y)$ are linear functions of y and x , respectively, whose values at the cell center are

$$\begin{aligned} (p_x^h)_{i+\frac{1}{2},j+\frac{1}{2}} &= \frac{1}{2[hx]} \{(p_{i+1,j} - p_{i,j}) + (p_{i+1,j+1} - p_{i,j+1})\}, \\ (p_y^h)_{i+\frac{1}{2},j+\frac{1}{2}} &= \frac{1}{2[hy]} \{(p_{i,j+1} - p_{i,j}) + (p_{i+1,j+1} - p_{i+1,j})\}. \end{aligned}$$

Thus, making the additional assumption that the *east/west* stencil weights are approximately constant functions of y , we obtain

$$\mathcal{F}_{i+\frac{1}{2},j+\frac{1}{2}}^E \approx \frac{1}{hy} \overline{S}_{i,j}^E \left[(p_x^h)_{i+\frac{1}{2},j+\frac{1}{2}} hx \right] = \frac{hx}{hy} \overline{S}_{i,j}^E (p_x^h)_{i+\frac{1}{2},j+\frac{1}{2}}.$$

Similarly, assuming that the *north/south* weights are approximately constant functions of x gives

$$\mathcal{F}_{i+\frac{1}{2},j+\frac{1}{2}}^N \approx \frac{1}{hx} \overline{S}_{i,j}^N \left[(p_y^h)_{i+\frac{1}{2},j+\frac{1}{2}} hy \right] = \frac{hy}{hx} \overline{S}_{i,j}^N (p_y^h)_{i+\frac{1}{2},j+\frac{1}{2}}.$$

The error associated with these expressions is $O(h^2)$ and, in particular, averaging the stencil coefficients is a second-order approximation. Averaging the fluxes directly would also provide an $O(h^2)$ approximation and differs from the above expressions only in the higher order terms,

$$\frac{1}{4} [(S_{i,j}^E - S_{i,j+1}^E)] (p_{xy}^h)_{i+\frac{1}{2},j+\frac{1}{2}} hx hy, \quad \frac{1}{4} [(S_{i,j}^N - S_{i+1,j}^N)] (p_{xy}^h)_{i+\frac{1}{2},j+\frac{1}{2}} hx hy,$$

respectively.

To extend this approach to the diagonal stencil weights, we introduce two rotated coordinate systems. The first, with coordinates (ξ_1, η_1) is shown in Fig. 14a and has ξ_1 aligned with the *northeast* diagonal of the cell. Thus, it has been rotated counterclockwise by an angle, $\theta = \tan^{-1}(hy/hx)$ and is related to (x, y) by the simple transformation,

$$\begin{bmatrix} x - x_{i+\frac{1}{2}} \\ y - y_{j+\frac{1}{2}} \end{bmatrix} = \begin{bmatrix} \cos(\theta) & -\sin(\theta) \\ \sin(\theta) & \cos(\theta) \end{bmatrix} \begin{bmatrix} \xi_1 \\ \eta_1 \end{bmatrix}. \quad (16)$$

The second coordinate system, (ξ_2, η_2) , shown in Fig. 14b, has been rotated counterclockwise by $(\pi/2 - \theta)$ to align η_2 with the *northwest* diagonal of the cell. The coordinates (ξ_2, η_2) are related to (x, y) by the simple transformation,

$$\begin{bmatrix} x - x_{i+\frac{1}{2}} \\ y - y_{j+\frac{1}{2}} \end{bmatrix} = \begin{bmatrix} \sin(\theta) & -\cos(\theta) \\ \cos(\theta) & \sin(\theta) \end{bmatrix} \begin{bmatrix} \xi_2 \\ \eta_2 \end{bmatrix}. \quad (17)$$

These coordinate systems are identical if $hx = hy$.

To approximate the fluxes, we first define the derivatives along the cell diagonals,

$$(p_{\xi_1}^h)_{i+\frac{1}{2},j+\frac{1}{2}} = p_{\xi_1}^h \Big|_{(x_{i+\frac{1}{2}}, y_{j+\frac{1}{2}})}, \quad (p_{\eta_2}^h)_{i+\frac{1}{2},j+\frac{1}{2}} = p_{\eta_2}^h \Big|_{(x_{i+\frac{1}{2}}, y_{j+\frac{1}{2}})}.$$

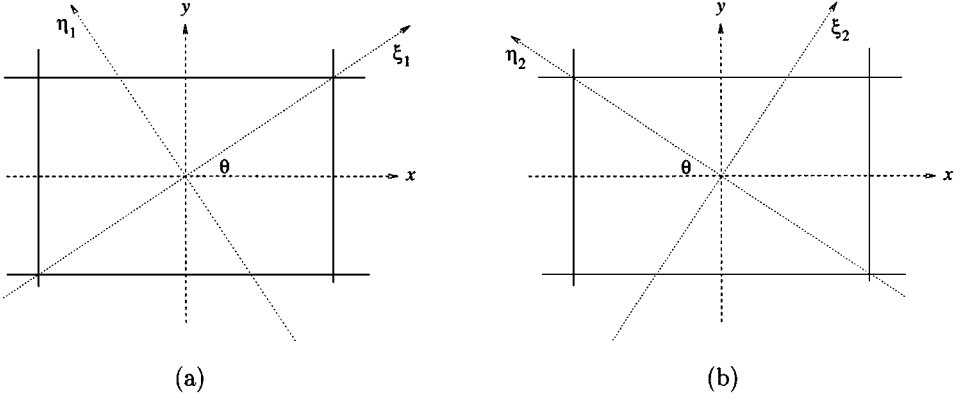


FIG. 14. Rotated coordinate systems: (a) (ξ_1, η_1) has ξ_1 aligned with the *northeast* diagonal of the cell, while (b) (ξ_2, η_2) has η_2 aligned with the *northwest* diagonal.

For a piecewise bilinear basis we have

$$\begin{aligned} (p_{\xi_1}^h)_{i+\frac{1}{2}, j+\frac{1}{2}} &= \frac{1}{h\xi_1} (p_{i+1, j+1} - p_{i, j}), \\ (p_{\eta_1}^h)_{i+\frac{1}{2}, j+\frac{1}{2}} &= \frac{1}{h\eta_2} (p_{i, j+1} - p_{i+1, j}). \end{aligned}$$

The cosine foreshortening of the interface as seen along the cell diagonals is depicted, for all four cases, in Fig. 15. Therefore, from Fig. 15 we have

$$\begin{aligned} \mathcal{F}_{i+\frac{1}{2}, j+\frac{1}{2}}^{NE(x)} &= \frac{S_{i,j}^{NE} \left[(p_{\xi_1}^h)_{i+\frac{1}{2}, j+\frac{1}{2}} h\xi_1 \right]}{[hy \cos(\theta)]} (\xi_1 \cdot \mathbf{x}) \\ &= \frac{hx}{hy \cos(\theta)} S_{i,j}^{NE} \left[\cos(\theta) (p_x^h)_{i+\frac{1}{2}, j+\frac{1}{2}} + \sin(\theta) (p_y^h)_{i+\frac{1}{2}, j+\frac{1}{2}} \right] \\ &= \frac{hx}{hy} S_{i,j}^{NE} (p_x^h)_{i+\frac{1}{2}, j+\frac{1}{2}} + S_{i,j}^{NE} (p_y^h)_{i+\frac{1}{2}, j+\frac{1}{2}}, \end{aligned}$$

and similarly,

$$\begin{aligned} \mathcal{F}_{i+\frac{1}{2}, j+\frac{1}{2}}^{NW(x)} &= \frac{S_{i+1,j}^{NW} \left[(p_{\eta_2}^h)_{i+\frac{1}{2}, j+\frac{1}{2}} h\eta_2 \right]}{[hy \cos(\theta)]} (\eta_2 \cdot \mathbf{x}) \\ &= -\frac{hx}{hy \cos(\theta)} S_{i+1,j}^{NW} \left[-\cos(\theta) (p_x^h)_{i+\frac{1}{2}, j+\frac{1}{2}} + \sin(\theta) (p_y^h)_{i+\frac{1}{2}, j+\frac{1}{2}} \right] \\ &= \frac{hx}{hy} S_{i+1,j}^{NW} (p_x^h)_{i+\frac{1}{2}, j+\frac{1}{2}} - S_{i+1,j}^{NW} (p_y^h)_{i+\frac{1}{2}, j+\frac{1}{2}}. \end{aligned}$$

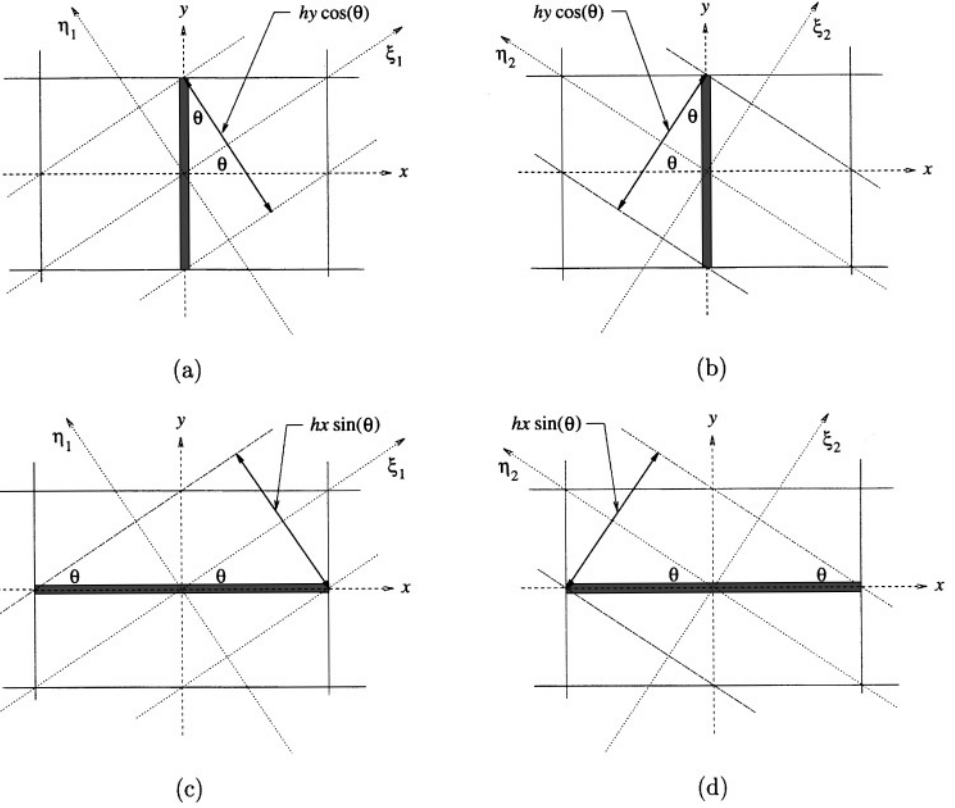


FIG. 15. Cosine foreshortening.

The evaluation of $\mathcal{F}_{i+\frac{1}{2},j+\frac{1}{2}}^{NE(y)}$ and $\mathcal{F}_{i+\frac{1}{2},j+\frac{1}{2}}^{NW(y)}$ follows analogously to yield

$$\begin{aligned}
 & \begin{bmatrix} \mathcal{F}_{i+\frac{1}{2},j+\frac{1}{2}}^{(x)} \\ \mathcal{F}_{i+\frac{1}{2},j+\frac{1}{2}}^{(y)} \end{bmatrix} \\
 &= \begin{bmatrix} \frac{hx}{hy} \{ \bar{S}_{i,j}^E + S_{i,j}^{NE} + S_{i+1,j}^{NW} \} & (S_{i,j}^{NE} - S_{i+1,j}^{NW}) \\ (S_{i,j}^{NE} - S_{i+1,j}^{NW}) & \frac{hy}{hx} \{ \bar{S}_{i,j}^N + S_{i,j}^{NE} + S_{i+1,j}^{NW} \} \end{bmatrix} \begin{bmatrix} (p_x^h)_{i+\frac{1}{2},j+\frac{1}{2}} \\ (p_y^h)_{i+\frac{1}{2},j+\frac{1}{2}} \end{bmatrix}.
 \end{aligned}$$

Direct comparison with the definition of anisotropic diffusion yields the permeability tensor $\widehat{\mathcal{K}}_{i+\frac{1}{2},j+\frac{1}{2}}$ given in Eq. (8). ■

A.2. An Exact Expression

We first assume that the permeability tensor is constant in Ω and is written

$$\mathcal{K}(x, y) \equiv \mathcal{K} = \mathcal{K}_{i+\frac{1}{2},j+\frac{1}{2}} = \begin{bmatrix} \mathcal{K}^{(x,x)} & \mathcal{K}^{(x,y)} \\ \mathcal{K}^{(x,y)} & \mathcal{K}^{(y,y)} \end{bmatrix},$$

so that the bilinear conforming finite element stencil weights are given by

$$\begin{aligned} S_{i,j}^E &= \frac{2}{3} \frac{hy}{hx} \mathcal{K}^{(x,x)} - \frac{1}{3} \frac{hx}{hy} \mathcal{K}^{(y,y)}, \\ S_{i,j}^N &= -\frac{1}{3} \frac{hy}{hx} \mathcal{K}^{(x,x)} + \frac{2}{3} \frac{hx}{hy} \mathcal{K}^{(y,y)}, \\ S_{i,j}^{NE} &= \frac{1}{6} \frac{hy}{hx} \mathcal{K}^{(x,x)} + \frac{1}{6} \frac{hx}{hy} \mathcal{K}^{(y,y)} + \frac{1}{2} \mathcal{K}^{(x,y)}, \\ S_{i,j}^{NW} &= \frac{1}{6} \frac{hy}{hx} \mathcal{K}^{(x,x)} + \frac{1}{6} \frac{hx}{hy} \mathcal{K}^{(y,y)} - \frac{1}{2} \mathcal{K}^{(x,y)}. \end{aligned}$$

Substitution into Eq. (8) immediately gives $\widehat{\mathcal{K}}_{i+\frac{1}{2},j+\frac{1}{2}} = \mathcal{K}_{i+\frac{1}{2},j+\frac{1}{2}}$. ■

APPENDIX B: INTERPOLATION

The order of the transfer operators in an efficient multigrid method must satisfy the well-known inequality

$$m_i + m_r > 2m,$$

where m_i and m_r are the order of the interpolation and the restriction, respectively, and $2m$ is the order of the PDE (see, e.g., [30, 31, 32]). If this condition is satisfied then variational coarsening generates coarse-grid operators that are relatively consistent [30], and typically consistent with the original PDE. However, if this condition is not satisfied, then an inconsistent coarse-grid discretization may arise and the multigrid method may be suboptimal. This result is demonstrated by de Zeeuw [33] for a constant coefficient second-order PDE.

Unfortunately, the situation for Eq. (1) with highly discontinuous permeability is more complicated because the regularity of the solution depends on the fine-scale structure of the permeability. Specifically, the gradient of the pressure may be discontinuous, in general, and it is the continuity of the normal flux (velocity) that must be preserved in the interpolation. In the following discussion we derive Dendy's [24] operator-induced interpolation and comment on its order of accuracy.

B.1. Fine Grid Stencil

In analogy with Appendix A, we adopt a flux-based analysis to derive Dendy's operator-induced interpolation [24]. Specifically, consider a fine-grid point that is embedded in a horizontal coarse-grid line (Fig. 16a). In this case we approximately enforce the continuity of the normal flux through the vertical face shown in Fig. 16. To simplify the notation we use (i, j) to index vertices and (k, l) to index cells (*i.e.*, $k = i + \frac{1}{2}$, $l = j + \frac{1}{2}$).

To derive the interpolation we consider preserving the continuity of the normal flux in a weak or integral sense,

$$\lim_{x \rightarrow x^-} \int_{y_{j-1}}^{y_{j+1}} (\mathcal{F} \cdot \mathbf{x}) dy = \lim_{x \rightarrow x^+} \int_{y_{j-1}}^{y_{j+1}} (\mathcal{F} \cdot \mathbf{x}) dy. \quad (18)$$

The contributions from each of the neighboring cells are defined by

$$(\mathcal{F} \cdot \mathbf{x})_{k,l}^{x_i^+} = \lim_{x \rightarrow x^+} \int_{y_{j-1}}^{y_{j+1}} (\mathcal{F} \cdot \mathbf{x}) dy, \quad (19)$$

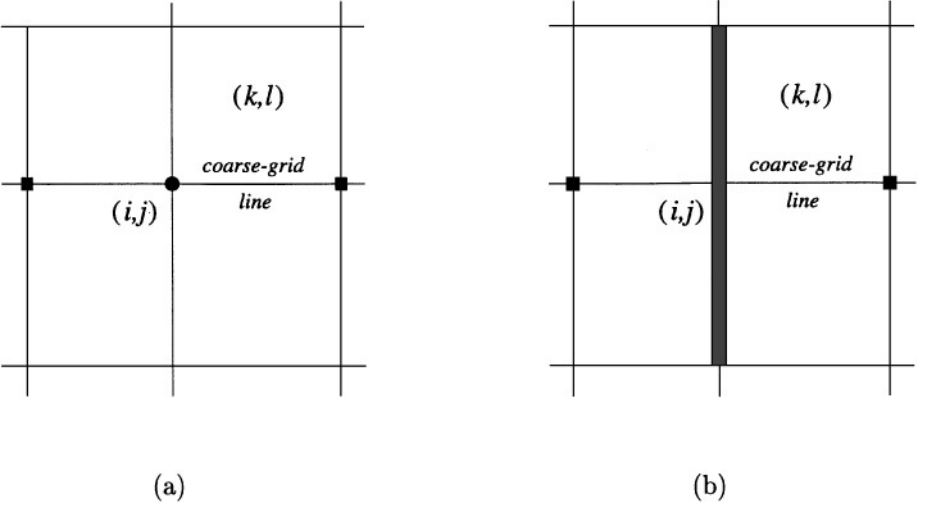


FIG. 16. (a) Interpolate the fine-grid point, “•,” from the coarse-grid points, “■.” (b) The objective is to preserve the continuity of the normal flux through the vertical interface at x_i (i.e., the shaded region).

with analogous definitions for the other cells. The continuity condition equation (18) can now be written in the form

$$(\mathcal{F} \cdot \mathbf{x})_{k-1,l}^{x_i^-} + (\mathcal{F} \cdot \mathbf{x})_{k-1,l-1}^{x_i^-} = (\mathcal{F} \cdot \mathbf{x})_{k,l}^{x_i^+} + (\mathcal{F} \cdot \mathbf{x})_{k,l-1}^{x_i^+}. \quad (20)$$

Following the approach of Appendix A we decompose each term in Eq. (20) into its stencil-based contributions; for example,

$$(\mathcal{F} \cdot \mathbf{x})_{k,l}^{x_i^+} = h y_l [\mathcal{F}_{k,l}^E + \mathcal{F}_{k,l}^{NE(x)} + \mathcal{F}_{k,l}^{SE(x)}]. \quad (21)$$

It is our objective to construct the interpolation weights from a single stencil. Thus we have

$$\mathcal{F}_{k,l}^E = \frac{1}{h y_l} \{S_{i,j}^E [(p_x)_{i,j}^{k,l} h x_k]\} \quad (22a)$$

$$\mathcal{F}_{k,l}^{NE(x)} = \frac{1}{h y_l} \{S_{i,j}^{NE} [(p_x)_{i,j}^{k,l} h x_k] + S_{i,j}^{NE} [(p_y)_{i,j}^{k,l} h y_l]\} \quad (22b)$$

$$\mathcal{F}_{k,l}^{SE(x)} = \frac{1}{h y_l} \{S_{i,j}^{SE} [(p_x)_{i,j}^{k,l} h x_k] + S_{i,j}^{SE} [(p_y)_{i,j}^{k,l} h y_l]\}. \quad (22c)$$

Substitution of Eqs. (22) into Eq. (20), along with analogous expressions for the other terms, yields a stencil-based continuity condition,

$$\begin{aligned} & (S_{i,j}^{SW} + S_{i,j}^{NW} + S_{i,j}^{SW}) [(p_x)_{i,j}^{k-1,l} h x_{k-1} + (p_x)_{i,j}^{k-1,l-1} h x_{k-1}] \\ & + (S_{i,j}^{SW} - S_{i,j}^{NW}) [(p_y)_{i,j}^{k-1,l} h y_l + (p_y)_{i,j}^{k-1,l-1} h y_{l-1}] \\ & = (S_{i,j}^E + S_{i,j}^{NE} + S_{i,j}^{SE}) [(p_x)_{i,j}^{k,l} h x_k + (p_x)_{i,j}^{k,l-1} h x_k] \\ & + (S_{i,j}^{NE} - S_{i,j}^{SE}) [(p_y)_{i,j}^{k,l} h y_l + (p_y)_{i,j}^{k,l-1} h y_{l-1}]. \end{aligned} \quad (23)$$

Unfortunately, incorporating the y -derivative into the interpolation is precluded by the desire to limit all coarse-grid operators to be 9-point operators. Thus, we assume that these terms are small, and hence, neglecting them we obtain

$$\begin{aligned} & (S_{i,j}^W + S_{i,j}^{NW} + S_{i,j}^{SW}) [(p_x)_{i,j}^{k-1,l} + (p_x)_{i,j}^{k-1,l-1}] h x_{k-1} \\ & = (S_{i,j}^E + S_{i,j}^{NE} + S_{i,j}^{SE}) [(p_x)_{i,j}^{k,l} + (p_x)_{i,j}^{k,l-1}] h x_k. \end{aligned} \quad (24)$$

Substitution of the one-sided differences

$$\begin{aligned} (p_x)_{i,j}^{x_i^+} &= (p_x)_{i,j}^{k,l} = (p_x)_{i,j}^{k,l-1} = \frac{1}{h x_k} (p_{i+1,j}^h - p_{i,j}^h) \\ (p_x)_{i,j}^{x_i^-} &= (p_x)_{i,j}^{k-1,l} = (p_x)_{i,j}^{k-1,l-1} = \frac{1}{h x_{k-1}} (p_{i,j}^h - p_{i-1,j}^h) \end{aligned}$$

into Eq. (24) yields

$$\begin{aligned} & (S_{i,j}^W + S_{i,j}^E + S_{i,j}^{NW} + S_{i,j}^{SW} + S_{i,j}^{NE} + S_{i,j}^{SE}) p_{i,j}^h \\ & = (S_{i,j}^W + S_{i,j}^{NW} + S_{i,j}^{SW}) p_{i-1,j}^h + (S_{i,j}^E + S_{i,j}^{NE} + S_{i,j}^{SE}) p_{i+1,j}^h. \end{aligned} \quad (25)$$

Recalling that $S_{i,j}^O = \sum_{* \neq O} S_{i,j}^*$ and switching to Dendy's cell-based symmetric notation reveals that Eq. (25) prescribes interpolation weights that are identical to those in Eq. (6).

B.2. The Order of Interpolation

To investigate the order of operator-induced interpolation we examine the approximation of the continuity condition that results from a specific fine-grid stencil. Specifically, consider a conforming bilinear finite element discretization of Eq. (1) with a piecewise constant diagonal permeability tensor

$$\mathcal{K}(x, y) = \mathcal{K}_{k,l} = \begin{bmatrix} \mathcal{K}_{k,l}^{(x,x)} & 0 \\ 0 & \mathcal{K}_{k,l}^{(y,y)} \end{bmatrix}$$

for all $(x, y) \in F_{k,l}$. Substitution of the stencil weights into Eq. (24) yields the continuity condition

$$\{\mathcal{K}_{k-1,l}^{(x,x)} h y_l + \mathcal{K}_{k-1,l-1}^{(x,x)} h y_{l-1}\} (p_x)_{i,j}^{x_i^-} = \{\mathcal{K}_{k,l}^{(x,x)} h y_l + \mathcal{K}_{k,l-1}^{(x,x)} h y_{l-1}\} (p_x)_{i,j}^{x_i^+} \quad (26)$$

with first-order one-sided difference approximations of $(p_x)_{i,j}^{x_i^-}$ and $(p_x)_{i,j}^{x_i^+}$.

This flux continuity condition incorporates an arithmetic treatment of $\mathcal{K}^{(x,x)}(x, y)$ in the y -direction (i.e., parallel to the vertical interface) and enforces the continuity of the normal flux across the vertical interface. Therefore, if the *local* structure of $\mathcal{K}(x, y)$ is either a horizontal or vertical interface the interpolation is second order. Unfortunately, estimating the order of interpolation for more general interface configurations is extremely difficult because the regularity of the solution depends on this property of the permeability.

REFERENCES

1. G. E. Pickup, P. S. Ringrose, J. L. Jensen, and K. S. Sorbie, Permeability tensors for sedimentary structures, *Math. Geol.* **26**(2), 227 (1994).
2. G. Dagan, *Flow and Transport in Porous Formations* (Springer-Verlag, New York/Berlin, 1989).
3. A. Bensoussan, J.-L. Lions, and G. Papanicolaou, *Asymptotic Analysis For Periodic Structures, Studies in Mathematics and its Applications*, Vol. 5 (North-Holland, New York, 1978).
4. V. V. Jikov, S. M. Kozlov, and O. A. Oleinik, *Homogenization of Differential Operators and Integral Functionals* (Springer-Verlag, New York/Berlin, 1994). [Translated from Russian]
5. D. S. Selengut, *Diffusion Coefficients for Heterogenous Systems*, Nuclear Physics Research Quarterly Report HW-60220, Hanford Laboratories, General Electric, Richland, Washington, April 1959.
6. X.-H. Wen and J. J. Gómez-Hernández, Upscaling hydraulic conductivities in heterogeneous media: An overview, *Journal of Hydrology* **183**, ix (1996).
7. C. Deutsch and A. G. Journel, *GSLIB: Geostatistical Software Library and User's Guide* (Oxford University Press, New York, 1992).
8. C. V. Deutsch and T. A. Hewett, Challenges in reservoir forecasting, *Math. Geol.* **28**(7), 829 (1996).
9. S. M. Kozlov, Averaging of random operators, *Math. USSR Sbornik* **37**, 167 (1980).
10. A. J. Desbarats, Spatial averaging of hydraulic conductivity in 3-dimensional heterogenous porous-media, *Math. Geol.* **24**(3), 249 (1992).
11. A. J. Desbarats, Spatial averaging of transmissivity in heterogeneous fields with flow toward a well, *Water Resour. Res.* **28**(3), 757 (1992).
12. L. J. Durlofsky, Representation of grid block permeability in coarse scale models of randomly heterogeneous porous-media, *Water Resour. Res.* **28**(7), 1791 (1992).
13. J. J. Gómez-Hernández and X.-H. Wen, Probabilistic assessment of travel times in groundwater modeling, *J. Stochastic Hydrology and Hydraulics* **8**(1), 19 (1994).
14. L. J. Durlofsky, Numerical-calculation of equivalent grid block permeability tensors for heterogeneous porous-media, *Water Resour. Res.* **27**(5), 669 (1991).
15. L. W. Lake, The origins of anisotropy, *Journal of Petroleum Technology*, 395 (1988).
16. J. J. Gómez-Hernández, *A Stochastic Approach to the Simulation of Block Conductivity Fields Conditioned Upon Data Measured at a Smaller Scale*, Ph.D. thesis, Stanford University, 1991.
17. L. Holden and O. Lia, A tensor estimator for the homogenization of absolute permeability, *Transport in Porous Media* **8**, 37 (1992).
18. E. Sanchez-Palencia, *Non-Homogeneous Media and Vibration Theory*, Lecture Notes in Physics, Vol. 127 (Springer-Verlag, Berlin, 1980).
19. M. H. Holmes, *Introduction to Perturbation Methods*, Texts in Applied Mathematics, Vol. 20 (Springer-Verlag, New York, 1995).
20. J. F. Bourgat, Numerical experiments of the homogenization method for operators with periodic coefficients, in *Computing Methods in Applied Science and Engineering, I, Versailles, December 5-9, 1977*, edited by R. Glowinski and J.-L. Lions (Springer-Verlag, New York/Berlin, 1978), p. 330.
21. P. R. King, The use of renormalization for calculating effective permeability, *Transport in Porous Media* **4**, 37 (1989).
22. K. M. Malick, Boundary effects in the successive upscaling of absolute permeability, Master's thesis, Stanford University, 1995.
23. R. E. Alcouffe, A. Brandt, J. E. Dendy Jr., and J. W. Painter, The multi-grid method for the diffusion equation with strongly discontinuous coefficients, *SIAM J. Sci. Stat. Comput.* **2**(4), 430 (1981).
24. J. E. Dendy Jr., Black box multigrid, *J. Comput. Phys.* **48**, 366 (1982).
25. J. E. Dendy Jr., Black box multigrid for periodic and singular problems, *Appl. Math. and Comput.* **25**, 1 (1988).
26. S. Knapek, Matrix-dependent multigrid-homogenization for diffusion problems, in *The Preliminary Proceedings of the Copper Mountain Conference on Iterative Methods, Vol. I, SIAM Special Interest Group on Linear Algebra, Cray Research, April 9-13, 1996*, edited by T. Manteuffel and S. McCormick (SIAM, Philadelphia, 1996).

27. S. Knappek, Matrix-dependent multigrid-homogenization for diffusion problems, *SIAM J. Sci. Stat. Comput.*, to appear.
28. W. L. Briggs, *A Multigrid Tutorial* (SIAM, Philadelphia, 1987).
29. A. Brandt, Multi-level adaptive solutions to boundary-value problems, *Math. Comput.* **31**, 333 (1977).
30. W. Hackbusch, *Multi-Grid Methods and Applications*, *Springer Series in Computational Mathematics*, Vol. 4 (Springer-Verlag, Berlin, Heidelberg, 1985).
31. A. Brandt, *Multigrid Techniques: 1984 Guide with Applications to Fluid Dynamics* (The Weizmann Institute of Applied Science, Rehovot, Israel, 1984).
32. P. W. Hemker, On the order of prolongations and restrictions in multigrid procedures, *J. Comp. Appl. Math.* **32**, 423 (1990).
33. P. M. de Zeeuw, Development of semi-coarsening techniques, *Appl. Num. Math.* **19**, 433 (1996).